PAPER

MRI simulation: end-to-end testing for prostate radiation therapy using geometric pelvic MRI phantoms

IOP Publishing | Institute of Physics and Engineering in Medicine Physics in Medicine & Biology

Phys. Med. Biol. **60** (2015) 3097–3109 doi:10.1088/0031-9155/60/8/3097

MRI simulation: end-to-end testing for prostate radiation therapy using geometric pelvic MRI phantoms

Jidi Sun[1,6], Jason Dowling[2], Peter Pichler[3], Fred Menk[1], David Rivest-Henault[2], Jonathan Lambert[1,4], Joel Parker[3], Jameen Arm[5], Leah Best[5], Jarad Martin[1,3], James W Denham[1,3] and Peter B Greer[1,3]

[1] School of Mathematical and Physical Sciences, University of Newcastle, Newcastle, New South Wales, Australia
[2] CSIRO Australian E-Health Research Centre, Brisbane, Queensland, Australia
[3] Department of Radiation Oncology, Calvary Mater Newcastle, Newcastle, New South Wales, Australia
[4] Department of Radiation Oncology, Radiation Oncology Institute, Gosford, NSW, Australia
[5] Department of Radiology, Hunter New England Health, Calvary Mater Newcastle, NSW, Australia

E-mail: jidi.sun@uon.edu.au

Received 27 October 2014, revised 12 February 2015
Accepted for publication 19 February 2015
Published 24 March 2015

Abstract

To clinically implement MRI simulation or MRI-alone treatment planning requires comprehensive end-to-end testing to ensure an accurate process. The purpose of this study was to design and build a geometric phantom simulating a human male pelvis that is suitable for both CT and MRI scanning and use it to test geometric and dosimetric aspects of MRI simulation including treatment planning and digitally reconstructed radiograph (DRR) generation.

A liquid filled pelvic shaped phantom with simulated pelvic organs was scanned in a 3T MRI simulator with dedicated radiotherapy couch-top, laser bridge and pelvic coil mounts. A second phantom with the same external shape but with an internal distortion grid was used to quantify the distortion of the MR image. Both phantoms were also CT scanned as the gold-standard for both geometry and dosimetry. Deformable image registration was used to quantify the MR distortion. Dose comparison was made using a seven-field IMRT plan developed on the CT scan with the fluences copied to the MR image and recalculated using bulk electron densities.

[6] Author to whom any correspondence should be addressed. Radiation Oncology, Calvary Mater Newcastle, Locked Bag 7, Hunter Region Mail Centre NSW 2310, Australia

Without correction the maximum distortion of the MR compared with the CT scan was 7.5 mm across the pelvis, while this was reduced to 2.6 and 1.7 mm by the vendor's 2D and 3D correction algorithms, respectively. Within the locations of the internal organs of interest, the distortion was <1.5 and <1 mm with 2D and 3D correction algorithms, respectively. The dose at the prostate isocentre calculated on CT and MRI images differed by 0.01% (1.1 cGy). Positioning shifts were within 1 mm when setup was performed using MRI generated DRRs compared to setup using CT DRRs.

The MRI pelvic phantom allows end-to-end testing of the MRI simulation workflow with comparison to the gold-standard CT based process. MRI simulation was found to be geometrically accurate with organ dimensions, dose distributions and DRR based setup within acceptable limits compared to CT.

Keywords: prostate cancer, radiotherapy treatment planning, MRI simulation

(Some figures may appear in colour only in the online journal)

1. Introduction

Prostate radiation therapy planning is often performed using computed-tomography (CT) scans co-registered with magnetic resonance imaging (MRI) scans. The high contrast MRI scan provides prostate and potentially other organ contours while the CT scan is used for dose calculation and digitally reconstructed radiograph (DRR) generation. There would be benefits from an MRI-only treatment planning procedure for prostate radiotherapy. Co-registration errors of the prostate contour would be eliminated, patient workflow would be streamlined, and scan costs reduced. It has been estimated that spatial uncertainties would be reduced from 3–4 mm with CT-MR registration to 2–3 mm with MRI alone planning (Jonsson *et al* 2010). The (albeit small) radiation dose from CT would also be reduced. However, geometric distortions in MRI images could lead to prostate, organ contour and external body contour inaccuracies, and hence dosimetric errors, and errors in DRRs and patient setup. Another problem is that the MRI image pixel values cannot be used to calculate dose, although this is being addressed by electron-density mapping methods (Beavis *et al* 1998, Lee *et al* 2003).

To examine and test aspects of the MRI simulation planning process a variety of approaches have been used. Phantoms have been used to quantify the spatial distortion of the MRI scans compared with CT (Lee *et al* 2003, Wang *et al* 2004, Doran *et al* 2005, Baldwin *et al* 2007, Stanescu *et al* 2010). In general these studies have not used phantoms of sufficient size to fully determine spatial resolution for pelvic MRI simulation. Comparisons have also been made between organ and external contour dimensions on CT and MRI images for the same patients (Chen *et al* 2004, Greer *et al* 2011, Lambert *et al* 2011), and positions of gold-markers identified on MRI have been investigated (Kapanen *et al* 2013). The accuracy of MRI generated DRRs has been investigated by Chen *et al* (2007).

This current work developed MRI compatible pelvic-shaped phantoms to simulate an average patient geometry, including external contour, internal organs and gold fiducial markers. There were two aims: 1) to quantify distortion for pelvic MRI scanning using an improved deformable registration method; and 2) to develop end-to-end testing procedures for the MRI simulation process, with validation against the conventional CT based process.

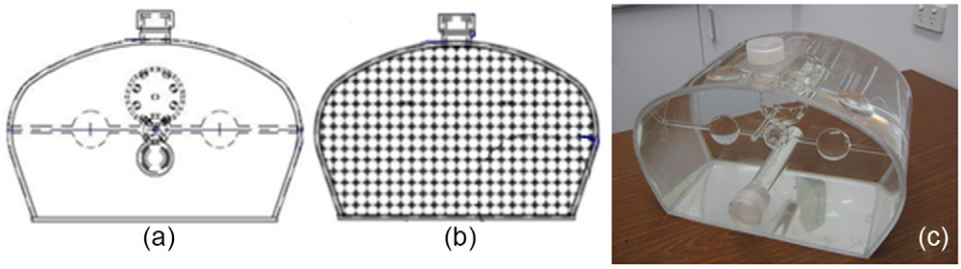

Figure 1. Schematics of the pelvic MRI phantom that is structured with the organs of interest, Phant-A (*a*) and the one that has parallel grid sheets inserted for the distortion quantification, Phant-B (*b*). A photo of Phant-A is shown in (*c*).

2. Methods

2.1. Phantom design

A custom built pelvic-shaped phantom (Phant-A) was designed (25.0 cm height, 40.0 cm width, and 26.0 cm length). Spherical and cylindrical Perspex (polymethylmethacrylate, PMMA) structures representing the prostate, rectum, bladder, and femoral heads were included in the design (figure 1(*a*)). The external and internal dimensions and locations of these organs were based on average values obtained from 39 patient CT scans used in a separate study (Lambert *et al* 2011). The prostate was represented by a hollow central sphere of radius 2.1 cm, which was supported by Perspex rods. The prostate has three gold seeds attached to the outside. The isocentre or (0, 0, 0) position of the phantom is at the centre of the prostate, which was 12.7 cm from the bottom and at the midline of the phantom length. The same rods also supported two extra solid spheres of radius 2.5 cm spaced 17.6 cm apart along the midline to represent the femoral heads. The bladder was represented by a large 8 cm diameter hollow sphere and was placed such that the centre was 16.6 cm from the bottom of the phantom. The rectum was represented by a hollow air-filled cylinder running from the front to the back of the phantom, situated underneath the central sphere. The rectum was filled with air to simulate the possibility of the presence of air in the rectum (rather than assuming an air equivalent density when applying the density overrides), however it can also be fluid filled if required.

In order to obtain the distortion information, a second phantom (Phant-B) with the same external dimensions was built which contained 11 plastic grid sheets positioned parallel to each other. The design of the grid sheet follows that of Wang *et al* 2004. Both phantoms were filled with mineral oil to avoid artefacts due to the dielectric effect when scanning at 3T field strength Schick 2005. Both phantoms have orthogonal lines engraved on the external surface for positioning.

2.2. Scan acquisition

CT scans were performed with a GE LightSpeed RT 4-slice helical scanner (GE Medical Systems, Milwaukee, USA), with scans performed at 2 mm slice thickness. Phant-B was CT scanned while it was empty in order to achieve maximum grid contrast. The MRI scanner was a Skyra 3T scanner (Siemens Medical, Erlingen, Germany) with dedicated radiation therapy (RT) couch-top and coil mounts manufactured by CIVCO (CIVCO, Iowa, USA). The coil mount consists of two arches or bridges that are used to position the pelvic imaging coil above the patient skin surface so as not to distort the patient contour. MRI sequences of the phantom

Table 1. MRI scan acquisition parameters.

	Matrix	Pixel Size (mm)	TR (ms)	TE (ms)	Flip angle (°)	Time (min)
'Planning', 3D LFOV	256 × 256 × 128	1.6 × 1.6 × 1.6	1200	101	135	5:41
Contouring, 3D SFOV	320 × 320 × 60	0.6 × 0.6 × 2	1400	97	135	3:55
Gold seeds 2D T2*w GRE	320 × 320 × 60	0.6 × 0.6 × 2	690	14	25	3:06

were acquired using our clinical scanning parameters listed in table 1. These consisted of: 1) a T_2 scan sequence with a field of view (FOV) encompassing the entire phantom; 2) a T_2 small FOV of 20 cm encompassing the prostate only; and 3) a T_2* sequence for imaging the gold fiducials. The phantoms were positioned using a CT and MR room positioning laser bridge (LAP Laser, Luneburg, Germany).

2.3. Distortion quantification

The vendor's 3D distortion correction algorithm was used for the acquisition of Phant-A. Phant-B was acquired three times: without distortion correction and with 2D and 3D distortion correction. The CT image was used as the gold standard and instead of comparing the coordinates of only the intersection of grids in Phant-B (Wang *et al* 2004, Stanescu *et al* 2010), the registration method was used to include sampling points between two intersections, thus giving finer distortion measurement resolution. The MR image was originally registered to the CT image (figure 2(*a*)) using the entire phantom, but the external surface intensity disagreement (Perspex does not give a strong signal in MR images) resulted in a large error in the deformable registration. Therefore both MR and CT images were masked initially to exclude the outer Perspex region (figures 2(*b*) and (*c*)). Because the intensity distribution was different on the two images (plastic appears bright on CT but dark on MR image), the intensity on the MR image was normalised to be consistent with the intensity distribution on CT image by reversely assigning the intensity values to different groups of objects on the MR image (figure 2(*d*)). The MRI scans with no distortion correction, 2D distortion correction and 3D distortion correction applied were registered to the CT image to quantify the distortion of the scanner and the residual distortion after using the vendor's correction algorithms. Rigid registration (Insight Toolkit versorRigid3D Transform, Mattes Mutual Information metric, regular gradient descent optimizer) was performed to align the images prior to deformable registration.

The free form deformation (FFD) was used for deformable registration (Sederberg and Parry 1986, Rueckert *et al* 1999). FFD is a technique which performs the deformation not directly on the object itself but on a virtual grid frame. A grid structure with the specified number of control points ($l + 1$, $m + 1$ and $n + 1$ in each direction) is created around the object. The coordinate system is set up obeying the following equation:

$$\boldsymbol{X} = \boldsymbol{X}_0 + \mathrm{s}\boldsymbol{S} + \mathrm{t}\boldsymbol{T} + \mathrm{u}\boldsymbol{U}$$

where $\boldsymbol{X}$ is any point within the coordinate, $\boldsymbol{X}_0$ is the coordinate origin, $\boldsymbol{S}$, $\boldsymbol{T}$ and $\boldsymbol{U}$ are the three orthogonal coordinates of the *global* coordinate system and s, t and u are the coordinates of the *local* lattice space, with value within (0, 1). The local lattice space allows the pixels within the control points to deform in order to improve the smoothness.

The control points located on the lattice can be guided by the following equation, where $i = 0..l$, $j = 0..m$ and $k = 0..n$.

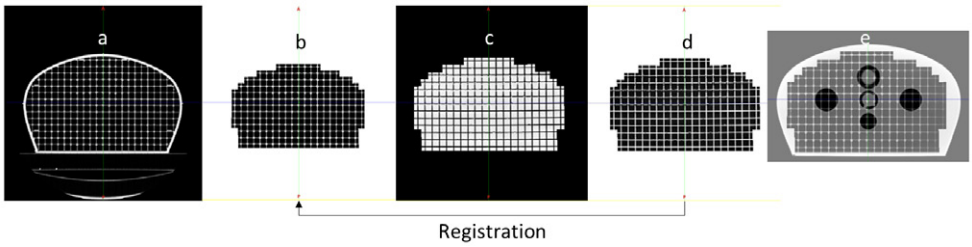

Figure 2. Phant-B registration process. (*a*) original CT image; (*b*) masked CT image; (*c*) masked MR image; (*d*) MR image normalised to CT intensity distribution; (*e*) Phant-A and B fused together in order to find distortion within ROIs.

$$\boldsymbol{P}_{i,j,k} = \boldsymbol{X}_0 + \frac{i}{l}\boldsymbol{S} + \frac{j}{m}\boldsymbol{T} + \frac{k}{n}\boldsymbol{U}$$

The deformed location of $\boldsymbol{X}'$ can be calculated by the trivariate Bernstein polynomial, B, as follows:

$$\boldsymbol{X}' = \sum_{i}^{l}\sum_{j}^{m}\sum_{k}^{n}\boldsymbol{P}_{i,j,k}B_i(s)B_j(t)B_k(u)$$

The deformation field vector image gives the distortion on the MR image. Phant-B quantifies the general distortion within the pelvic region and in order to find the distortion effect on the organ structures, while ROIs (region of interest) on Phant-A were used to mask the deformation field vector image by overlapping the images of the two phantoms (figure 2(*e*)). The organ structures were contoured on the Phant-A image in the Eclipse treatment planning software (Varian Medical Systems, Palo Alto, CA, USA, Version 11). Details of the contouring process will be discussed in next two sections. The deformation field vector image was masked by the organ contours to give the distortion within the locations of the organs of interest.

2.4. Contour generation

The external contour of the phantom was automatically identified separately on CT and MRI. Adjustment was made for the thickness of the external Perspex wall of the phantom which was not visible on the MRI scans, by adding an additional 5 mm expansion to the MRI body contour, which is the physical thickness of the phantom wall. The external body contour was limited to 14 cm in total length in the superior–inferior direction to avoid the filling cap of the phantom.

Contours of the spherical prostate, bladder and femoral heads on Phant-A were then created using the spherical contour tool of the Eclipse system. The known diameters of the objects were used to define the spheres, which were then manually positioned on the organs using the centre axial slice. This was necessary as manually contouring the objects was found to be inaccurate. The borders visible on the MRI and CT scans were different for the objects and the borders had very low contrast on the CT scans. For the rectum a circular contouring tool of the correct diameter was used and this was interpolated. The length of the rectum contoured in each scan was the same. The fiducial markers attached to the prostate were manually contoured by a radiation therapist on CT and T_2* MR images. CT and MRI images of the phantoms are shown in figure 3. Because of the invisibility of the phantom case surface, the body contour was expanded on the MR image.

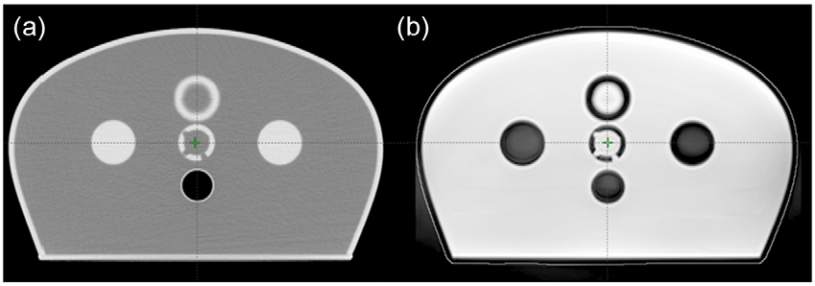

Figure 3. CT (*a*) and MR (*b*) images of the phantom. The external plastic wall/air body contour is not visible on the MRI scan and the added contour expansion (white line) is shown.

2.5. Dose calculation

A seven field IMRT plan was created on the CT in Eclipse. The spherical prostate contour was defined as CTV (clinical target volume). A 7 mm margin was added to the CTV to create the PTV (planning target volume). The isocentre was defined as the centre of the CTV (prostate). Field angles were 150°, 100°, 60°, 0°, 300°, 260°, and 210°. A 6 MV energy machine with 45° collimator rotation was used because collimator rotation is commonly used to reduce the effects of inter-leaf leakage on the plans. Target dose constraints were used to deliver 7800 cGy in 39 fractions ($D_{98\%} \geq 100\%$, $D_{2\%} \leq 105\%$). To create the MRI simulation plan, the same beams and fluences were copied to the MRI scan with the isocentre at the centre of the CTV. A new plan was not generated from scratch on the MRI scan as the optimisation process will always introduce MU differences into the plans, even when calculated on the same scan. The bulk electron density method was used for dose calculation. Both plans were calculated with densities of 288 HU applied to the femoral heads (calculated as an appropriate density from a previous study (Lambert *et al* 2011)), −1000 HU (air) applied to the air-filled rectum, and all other tissue assigned to 0 HU (water-equivalent). Consequently, the only difference between the two images lay in the geometry. The purpose was not to test the effect of differences in dose calculation due to HU assignment methods to MRI as these have been established in other reports (Lee *et al* 2003, Chen *et al* 2004, Jonsson *et al* 2010).

Doses on the MRI simulation plan were calculated and compared to the CT using DVH comparisons. Parameters used for the plan evaluation include: conformal index (CI), homogeneity index (HI) and quality index (QI) (Wang *et al* 2005, Sheng *et al* 2007, Lee *et al* 2008). CI is defined as the ratio of the PTV prescribed dose volume to the total PTV volume. HI is defined as the ratio of $D_{5\%}$ to $D_{95\%}$. QI is defined as the ratio of maximal organ at risk doses of MR and CT plans, QI is unity for best MR plan quality.

2.6. DRR generation and treatment positioning

DRRs were generated based on the manual seed contours drawn on the CT and MRI images by the radiation therapist. The linear accelerator (linac) was a Varian Trilogy with an on-board kilovoltage imaging unit and cone-beam CT reconstruction software (Varian Medical Systems, Palo Alto, CA, USA). The phantom was aligned on the treatment couch and orthogonal kilovoltage images acquired with the on-board imaging system according to standard prostate seed imaging protocols. The required shift in alignment was calculated based on manual registration of both CT based and MRI based DRRs and the orthogonal x-ray images. The

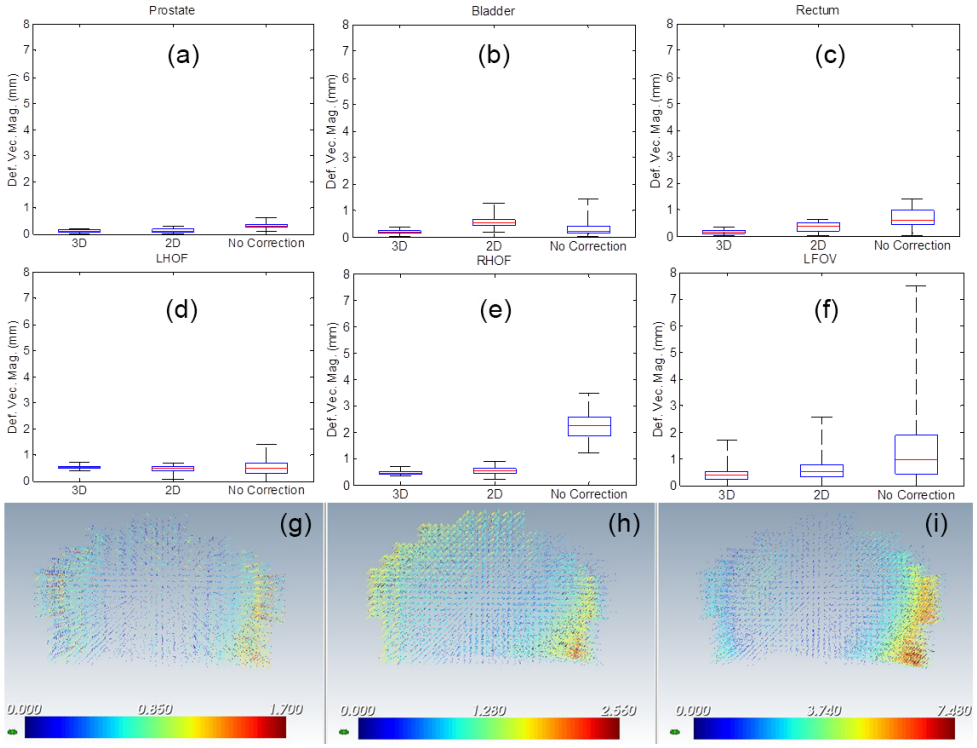

Figure 4. DVM within organs of interest structures (*a*)–(*e*) and within the entire phantom (*f*) by registering 3D and 2D corrected MR images and image without correction back to the CT image. The deformation vectors for 3D, 2D and no correction images are plotted in (*g*)–(*i*). The deformation vector unit is in mm.

MRI image was also input to the system for registration to a cone-beam CT (CBCT) scan of the phantom. This required modification of the DICOM header entry so that the image was recognised by the registration software as a 'CT' image.

3. Results

3.1. Distortion quantification

The deformation field vector images were masked with organs of interest contours to give the distortion near the critical organs (figure 2(*e*)) and each deformation result is shown in figures 4(*a*)–(*e*). The deformation vector magnitude (DVM) within the entire phantom region was also plotted (figure 4(*f*)). The maximum DVM across the entire phantom was 1.7 mm (median: 0.37 mm, 75% quartile: 0.54 mm), 2.6 mm (median: 0.54 mm, 75% quartile: 0.78 mm) and 7.5 mm (median: 0.96 mm, 75% quartile: 1.88 mm) for the three images, 3D, 2D and no correction respectively (figures 4(*f*)–(*i*)). The distortion within the prostate was minimal because it was located at the isocentre of the scanner. The range of distortion within smaller organ structures, e.g. prostate, was relatively smaller than within larger organ structures, which occupy regions further away from the isocentre. Among the three images, the 3D corrected image resulted in the smallest maximum distortion. The asymmetrical DVM between two HOFs (head of femurs; figures 4(*d*) and (*e*)) may be the result of machine-induced distortion,

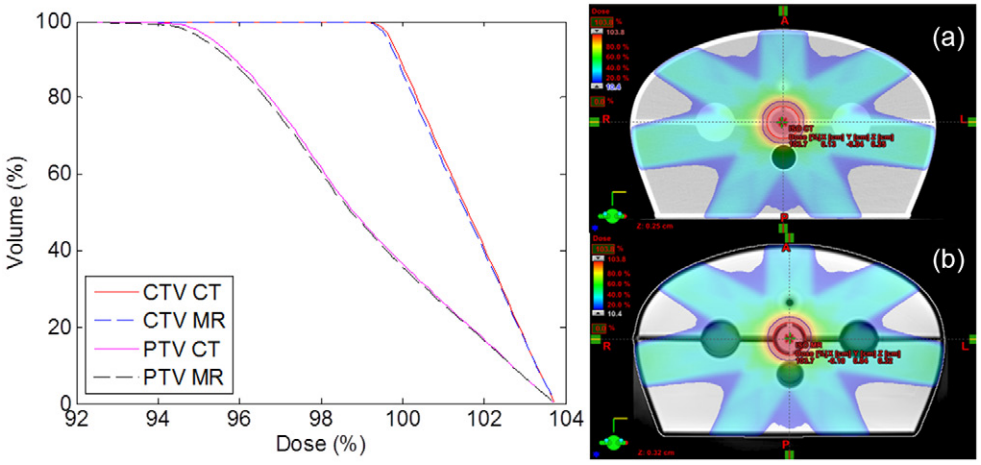

Figure 5. CTV and PTV DVH comparison between plans generated based on CT and MR images (left) and the comparison of CT (*a*) and MRI (*b*) dose distributions in the axial isocentre slice.

Table 2. Dose-volume comparison between the reference CT plan and the duplicated MR plan, HI, CI of PTV.

	CTV D_{95}	CTV D_2	PTV D_{95}	PTV D_2	HI	CI
MR	99.6 ± 0.0%	103.7 ± 0.1%	95.1 ± 0.3%	103.5 ± 0.0%	1.1 ± 0.0	35.7 ± 0.0%
CT	99.6 ± 0.1%	103.7 ± 0.0%	95.2 ± 0.2%	103.5 ± 0.0%	1.1 ± 0.0	36.4 ± 0.1%

e.g. uneven gradient field. However, this distortion was corrected to within 1.5 mm by the 2D correction algorithm and to within 1 mm by the 3D correction algorithm. Comparing to the uncorrected image, 3D correction reduced the maximum distortion by 73, 67, 79, 50 and 80% at the bladder, prostate, rectum, LHOF and RHOF, respectively.

The registration accuracy was evaluated by comparing the locations of the same grid intersection on the registered MR image and CT image. The ideal registration should result in zero difference. After the registration, no visual spatial difference was observed on the 2D and 3D corrected images compared with the CT image. On the registered MR image whose distortion had not been corrected, no visual spatial difference was observed except on the two grid sheets located near the phantom edges. Of all the grid intersections (239 in total on each sheet), visual spatial difference was observed at only 44 and 38 intersections. Of the intersections observed with differences on the two peripheral sheets, the spatial difference was 1.7 ± 0.6 and 1.1 ± 0.6 mm, respectively. The maximum difference of 4.7 mm was observed at the intersection located at the posterior corner edge of one sheet, where the most distortion was observed (figure 4(*i*)). The difference observed at the two edge sheets is mainly due to the large level of distortion that causes challenges in the registration.

We used a robust inverse-consistent registration algorithm to align the CT and MR images. This algorithm handles the position and orientation information contained in the image header and provided us with a fully automatic result. This algorithm is succinctly described in a recent conference paper and we are currently preparing a more detailed journal paper (Rivest-Hénault *et al* 2014).

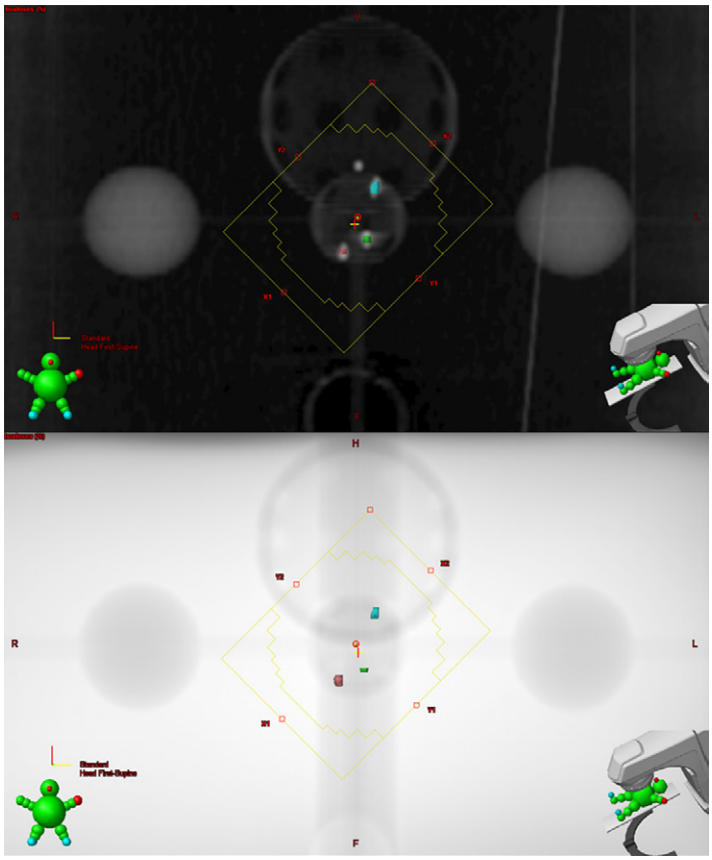

Figure 6. CT (top) and MR (bottom) DRR with seed contours (view from 0°). The fiducial markers on MR image were initially contoured on the T_2* image.

3.2. Dose calculation

The workflow was repeated by five instances (days), in which the organs were repeatedly delineated on MR and CT images and the dose was repeatedly calculated. Comparisons of the DVHs for the PTV and CTV are shown in figure 5. The mean point dose at the centre of the target was 8127.3 ± 0.9 and 8126.2 ± 0.6 cGy on the MR and CT plans, respectively. For PTV, D_{95} has difference of 0.1%, 7.8 cGy, while no difference was observed within CTV (table 2). Axial views of the two dose distributions through the isocentre plane are shown in the right hand panels of figure 5. No difference was found for HI between the two plans but the MR plan is slightly (0.7%) less conformal than the CT plan. The QI is unity for bladder and HOFs and the MR plan delivers 1% more dose to rectum compare to the CT plan.

3.3. DRR generation and treatment positioning

DRRs were generated from CT and MR images, as illustrated in figure 6, which shows how the MR image can be used to create a DRR for treatment planning, using marker contours projected onto the DRR. The markers were contoured on the T_2* MR image and then registered onto the T2 MR image. The accuracy of the marker contouring was demonstrated by setting

Table 3. Couch shift (cm) as per OBI (on-board imager) software for pre- and post-treatment isocentre position.

Method	Vertical	Longitudinal	Lateral
CT DRR kV	0	0	0
MR DRR kV	0	−0.1	0
CBCT	−0.1	0.1	0

up the phantom on the linac. The couch shifts based on the locations of markers on the DRRs are summarised in table 3. These are the shifts derived from the treatment setup registration software based on the imported CT-based DRR, the imported MRI-based DRR, and from the CBCT registration. No visible organ structure difference was observed after the registration based on the markers.

4. Discussion

End-to-end testing of the radiotherapy planning process is usually performed with phantoms. Solid phantoms present in most departments are not suitable for the assessment of MRI simulation as the solid materials do not give a signal on MRI. Our phantom was custom designed to the shape of the human pelvis and was able to present organ structures with the corresponding signal on MR: brighter signals for bladder and prostate, low signals for HOFs and zero signal for rectum. In addition, a grid phantom was also constructed to quantify the distortion of the MR images within the pelvic region.

The image registration approach was used to quantify MR image distortion by comparing it to the reference CT image. Without the distortion correction algorithm, the maximum distortion across the pelvic region was 7.5 mm (75% quartile: 1.88 mm), while the 2D and 3D correction algorithms were able to reduce the distortion to 2.6 mm (75% quartile: 0.78 mm) and 1.7 mm (75% quartile: 0.54 mm), respectively. For the organs of interest, the residual distortion on the 3D corrected image was less than 1 mm, which is acceptable for radiotherapy contouring (Kutcher *et al* 1994). It needs to be noted here that by applying organ masks from one phantom image to another, we assumed that the geometric distortions on the two images were equivalent.

Unlike previous distortion studies which first determined the physical grid intersections as the control points (Wang *et al* 2004, Baldwin *et al* 2007, Stanescu *et al* 2010), the MR distortion in this study was quantified using solely the deformable image registration method. One benefit of this approach is that it removes error which could occur when searching for physical grid intersection locations. A further benefit is that the number of defined control points is more flexible and not limited to the finite number of physical grid intersections (although information between two grid intersections can still be used for the distortion quantification). The physical control points available on figure 2 are 5258 (239 on each of 11 grid sheets). By reducing the sampling space registration by half on each grid sheet, 94.6% more control points are available (10230 in total). The image registration method used in this study is a suitable alternative method to quantify the overall geometric distortion. However, there may be a more robust method to quantify the distortion from a specific cause. For example, the distortion induced by the B0 field inhomogeneity can be quantified by evaluating the field map from a dual-echo gradient echo sequence of the phantom, which is a more robust method in this case (Jezzard and Balaban 1995, Andersson *et al* 2001, Hutton *et al* 2002). There is one limitation in our study: the geometric distortion quantified was only machine-induced and it did not include the patient-induced distortion.

Finally, the organ contours were given bulk electron densities and an IMRT plan was generated based on the CT image and then the same plan was copied to the MR image. There was no clinically significant dosimetric difference between the two plans (an average of 1.1 cGy dose difference in a 7800 cGy plan). This paper does not propose the use of bulk density for MR based planning; the purpose was to examine any differences in dose introduced by geometric differences of the phantom external shape and rectal and femoral head positions, which are the three major factors determining dose accuracy in pelvic planning. Many studies are currently underway to accurately map electron densities to MRI scans. Our group uses an atlas based approach, however this method is not suitable for mapping densities to phantoms which have a different MRI intensity distribution to patients. To assess the accuracy of the electron-density mapping component of MRI-Simulation requires comparison of densities mapped to MRI scans with CT densities for the same patients.

The grid phantom designed in this study is a useful tool to quantify MR geometric distortion for pelvic sites, such as prostate and cervix and can be used for routine quality assurance of the scanner for MR based planning. The MR anthropomorphic phantom was designed as an end-to-end test phantom in a similar way that plastic phantoms are used for CT based end-to-end tests. The MR phantom does not currently have positions for dosimeters and this would be a useful additional application, potentially the rectal air-filled tube could be used for this purpose with a specially designed insert. Other applications of the phantom could be for credentialing of sites for MR based planning in future clinical studies. It could be useful to determine the efficacy of new sequences such as ultra-short echo time (UTE) and pointwise echo time reduction with radial acquisition (PETRA) which both should image plastic water interfaces much more clearly than T2 sequences and are under intense investigation as sequences for MR based planning.

There are several suggestions to improve the current experiment and phantom design. First, the pelvic MR phantom does not assess several of the challenges in MR based planning such as motion artifacts and chemical shift artifacts. However chemical shift artifacts are unlikely to be a major challenge for pelvic planning, they will be important for head and neck MR applications. It is also not a useful tool for assessing electron density mapping uncertainties although it may have application in the assessment of ultra short sequences and their discrimination of air interfaces. In this study the same bulk density was applied to CT and MR images in this study in order to eliminate electron density uncertainties when comparing the dosimetry of CT- and MR-based plans. Electron density mapping using either multi-atlas (Dowling *et al* 2012, 2014) or regression (Johansson *et al* 2011) methods requires comparison of density and dose values between patient CT and synthetic CT scan pairs. These methods may introduce greater uncertainties than distortion however some reported dose agreements are very promising. Second, the phantom filling cap is located on the phantom anterior surface and has a height of 25 mm. This cap prevents the MR coil from being placed directly on the phantom surface; consequently the increased body-to-coil distance degrades the image quality. One solution is to reduce the height of the filling cap or relocate the cap to the side of the phantom. Third, three fiducial markers were implanted to the plastic prostate structure surface. Both materials gave low signal in MR images. One solution is to use wires to tie and position the seed inside the structure cavity, so that the intensity contrast between gold and oil maximises the distinguishability of seeds. Fourth, this study only acquired images from one day, but a scanner's physical variation may influence the geometric distortion over time. It would be more robust to repeat image acquisition over time in order to find the systematic variation of the scanner. Finally, the current phantom design is static. It will be more realistic if the phantom can simulate organ motion (e.g. prostate) with MR-compatible equipment.

5. Conclusions

In this study, the MR-based prostate treatment planning process was evaluated end-to-end using specially designed MRI compatible pelvic phantoms. The investigations included image distortion quantification, treatment planning system dosimetric accuracy, image guidance at the linear accelerator. The comparison was performed based on the reference CT scan as the gold standard. A deformable image registration method was used for the distortion quantification, with an increased flexibility of the control point definition allowing an increase in spatial resolution of distortion quantification. With the vendor's 3D distortion correction, the pelvis size MR image can be corrected to 1.7 mm maximal distortion with median of 0.37 mm (figure 4). By assigning bulk electron density, the treatment plan was calculated on CT and MR images and no clinically significant difference was found (0.01%, 1.1 cGy dosimetric difference). Setup of the phantom using MRI derived DRRs or CBCT was within 1 mm of CT based setup.

Acknowledgments

This research was partially funded by Cancer Council New South Wales research grant RG11-05 and the Prostate Cancer Foundation of Australia (Movember Young Investigator Grant YI2011) and Cure Cancer Australia. Author would like to thank James Talbot from the Auckland City Hospital, NZ for proofreading the manuscript.

References

Andersson J, Hutton C, Ashburner J, Turner R and Friston K 2001 Modeling geometric deformations in EPI time series *NeuroImage* **13** 903–19

Baldwin L, Wachowicz K, Thomas S, Rivest R and Fallone B 2007 Characterization, prediction, and correction of geometric distortion in 3T MR images *Med. Phys*. **34** 388–99

Beavis A, Gibbs P, Dealey R and Whitton V 1998 Radiotherapy treatment planning of brain tumours using MRI alone *Br. J. Radiol*. **71** 544–8

Chen L *et al* 2007 Magnetic resonance-based treatment planning for prostate intensity-modulated radiotherapy: creation of digitally reconstructed radiographs *Int. J. Radiat. Oncol. Biol. Phys*. **68** 903–11

Chen L, Price R A Jr and Nguyen T 2004 Dosimetric evaluation of MRI-based treatment planning for prostate cancer *Phys. Med. Biol.* **49** 5157–70

Doran S, Charles-Edwards L, Reinsberg S and Leach M 2005 A complete distortion correction for MR images: I gradient warp correction *Phys. Med. Biol*. **50** 1343–61

Dowling J A *et al* 2012 An atlas-based electron density mapping method for magnetic resonance imaging (MRI)-alone treatment planning and adaptive MRI-based prostate radiation therapy *Int. J. Radiat. Oncol. Biol. Phys*. **83** e5–11

Dowling J *et al* 2014 Automatic atlas based electron density and structure contouring for MRI-based prostate radiation therapy on the cloud *J. Phys. Conf. Ser*. **489** 012048

Greer P *et al* 2011 A magnetic resonance imaging-based workflow for planning radiation therapy for prostate cancer *Med. J. Aust*. **194** S24–7

Hutton C, Bork A, Josephs O, Deichmann R, Ashburner J and Turner R 2002 Image distortion correction in fMRI: a quantitative evaluation *NeuroImage* **16** 217–40

Jezzard P and Balaban R 1995 Correction for geometric distortion in echo planar images from B0 field variations *Magn. Reson. Med*. **34** 65–73

Johansson A, Karlsson M and Nyholm T 2011 CT substitute derived from MRI sequences with ultrashort echo time *Med. Phys*. **38** 2708–14

Jonsson J, Karlsson M, Karlsson M and Nyholm T 2010 Treatment planning using MRI data: an analysis of the dose calculation accuracy for different treatment regions *Radiat. Oncol*. **5** 62

Kapanen M, Collan J, Beule A, Seppälä T, Saarilahti K and Tenhunen M 2013 Commissioning of MRI-only based treatment planning procedure for external beam radiotherapy of prostate *Magn. Reson. Med*. **70** 127–35

Kutcher G *et al* 1994 Comprehensive QA for radiation oncology: report of AAPM radiation therapy committee task group 40 *Med. Phys*. **21** 581–618

Lambert J *et al* 2011 MRI-guided prostate radiation therapy planning: investigation of dosimetric accuracy of MRI-based dose planning *Radiother. Oncol*. **98** 330–4

Lee Y *et al* 2003 Radiotherapy treatment planning of prostate cancer using magnetic resonance imaging alone *Radiother. Oncol.* **66** 203–16

Lee T, Fang F, Chao P, Su T, Wang L and Leung S 2008 Dosimetric comparisons of helical tomotherapy and step-and-shoot intensity-modulated radiotherapy in nasopharyngeal carcinoma *Radiother. Oncol*. **89** 89–96

Rivest-Hénault D, Dowson N, Greer P and Dowling J 2014 Inverse-consistent registration of CT and MR for MR-based planning and adaptive prostate radiation therapy *J. Phys. Conf. Ser.* **489** 012039

Rueckert D, Sonoda L, Hayes C, Hill D, Leach M and Hawkes D 1999 Nonrigid registration using free-form deformations: application to breast MR images *IEEE Trans. Med. Imaging* **18** 712–21

Schick F 2005 Whole-body MRI at high field: technical limits and clinical potential *Eur. Radiol*. **15** 946–59

Sederberg T and Parry S 1986 Free-form deformation of solid geometric models *ACM Siggraph Comput. Graph.* **20** 151–60

Sheng K, Molloy J, Larner J and Read P 2007 A dosimetric comparison of non-coplanar IMRT versus helical tomotherapy for nasal cavity and paranasal sinus cancer *Radiother. Oncol*. **82** 174–8

Stanescu T, Jans H, Wachowicz K and Fallone B 2010 Investigation of a 3D system distortion correction method for MR images *J. Appl. Clin. Med. Phys*. **11** 2961

Wang X *et al* 2005 Effectiveness of noncoplanar IMRT planning using a parallelized multiresolution beam angle optimization method for paranasal sinus carcinoma *Int. J. Radiat. Oncol. Biol. Phys*. **63** 594–601

Wang D, Doddrell D and Cowin G 2004 A novel phantom and method for comprehensive 3D measurement and correction of geometric distortion in magnetic resonance imaging *Magn. Reson. Imaging* **22** 529–42